ENGINEERING

Robust and sensitive conductive nanocomposite hydrogel with bridge cross-linking–dominated hierarchical structural design

Tian Li[1], Haobo Qi[1], Yijing Zhao[1], Punit Kumar[2], Cancan Zhao[3], Zhenming Li[3], Xinyu Dong[1], Xiao Guo[1], Miao Zhao[1], Xinwei Li[1], Xudong Wang[3]*, Robert O. Ritchie[2]*, Wei Zhai[1]*

Conductive hydrogels have a remarkable potential for applications in soft electronics and robotics, owing to their noteworthy attributes, including electrical conductivity, stretchability, biocompatibility, etc. However, the limited strength and toughness of these hydrogels have traditionally impeded their practical implementation. Inspired by the hierarchical architecture of high-performance biological composites found in nature, we successfully fabricate a robust and sensitive conductive nanocomposite hydrogel through self-assembly–induced bridge cross-linking of MgB_2 nanosheets and polyvinyl alcohol hydrogels. By combining the hierarchical lamellar microstructure with robust molecular B—O—C covalent bonds, the resulting conductive hydrogel exhibits an exceptional strength and toughness. Moreover, the hydrogel demonstrates exceptional sensitivity (response/relaxation time, 20 milliseconds; detection lower limit, ~1 Pascal) under external deformation. Such characteristics enable the conductive hydrogel to exhibit superior performance in soft sensing applications. This study introduces a high-performance conductive hydrogel and opens up exciting possibilities for the development of soft electronics.

INTRODUCTION

Hydrogels have immense potential for various applications in biomedicine (1–3), energy storage (4), soft robotics (5, 6), and flexible electronics (7, 8). Nevertheless, a notable obstacle to their practical utilization is their limited strength (less than 1 MPa) (9, 10). Moreover, achieving an optimal combination of characteristics, such as high sensitivity, self-healing capability, and mechanical robustness, is crucial for the successful implementation of soft hydrogels in practical applications (11, 12).

The development of conductive hydrogels typically entails the integration of conductive components into the hydrogel matrix. These conductive phases encompass a variety of types such as nanomaterials [e.g., graphene (13), carbon nanotube (14), MXene (15–17), and Ag nanoparticles (18)], conductive ions [e.g., metal ions (9) and ionic liquid (19)], and conductive polymers [e.g., poly(3,4-ethylenedioxythiophene) polystyrene sulfonate (PEDOT:PSS) (20), polyaniline (PANI) (21), and polypyrrole (PPy) (22)]. It has brought to attention that often weak molecular bonds between the conductive phases and the hydrogel matrices, along with disordered structural distribution within the matrix, can adversely affect the mechanical properties of conductive hydrogels.

Biological soft tissues, such as tendon and cartilage, exhibit an exceptional combination of strength, flexibility, and message-passing ability, although they are composites based on simple compositions comprising biopolymers and minerals. For instance, the hierarchical organization of tendon endows them with high strength and flexibility, allowing them to endure mechanical stress and execute contractions and relaxations. Moreover, the interplay between message-passing proteins and other constituents within soft tissues contributes to their overall strength and sensing capabilities (23, 24). Inspired by the remarkable properties of bio-soft tissues, researchers have explored various structural and molecular engineering technologies to enhance the mechanical properties of hydrogels. Structural approaches, including freeze casting to create hierarchical structures (17, 25), stretch training to align hydrogel fibers (26), and salting out to induce strong chain aggregation (27, 28), have been extensively investigated. Molecular engineering approaches, including the formation of covalent bonds (29), hybrid networks (30), and nanocrystalline domains through annealing (31), have shown great potential in enhancing the mechanical strength of hydrogels. However, most of these engineering methods are "top-down" approaches that have limitations in creating strong bonding between hierarchical units after gelation (32).

Biological soft tissues are formed through the intricate process of cell division, which can be characterized as a "bottom-up" approach. A similar approach is observed in self-assembly, where physical driving forces are used to construct materials with ordered structures (33, 34). During self-assembly, the basic units gradually aggregate and become bulk materials with strong interface bonding. For instance, during the evaporation process, two-dimensional (2D) nanosheets in a solution effortlessly align under the influence of unidirectional solvent evaporation forces. Simultaneously, dehydration reactions occur between the hydroxyl groups of soluble hydroxyl-containing polymer molecules, leading to layer-by-layer crystallization of polymer molecules (35–37). To combine both structural and molecular engineering strategies, we incorporate 2D MgB_2 nanosheets as the electrical conductive phases within polyvinyl alcohol (PVA) hydrogel matrix and create them into nanocomposite hydrogels through a simple self-assembly–induced boron bridging method. Structurally, the evaporation approach facilitates the layer-by-layer self-assembly of PVA and MgB_2 nanosheet layers into a lamellar microstructure. Meanwhile, MgB_2 nanosheets can serve as high-functionality cross-links, forming a large number of

[1]Department of Mechanical Engineering, National University of Singapore, Singapore 117575, Singapore. [2]Department of Materials Science & Engineering, University of California, Berkeley, Berkeley, CA 94720, USA. [3]Department of Oral and Cranio-Maxillofacial Surgery, Shanghai Ninth People's Hospital, College of Stomatology, Shanghai Jiao Tong University School of Medicine; National Clinical Research Center for Oral Diseases; Shanghai Key Laboratory of Stomatology & Shanghai Research Institute of Stomatology, Shanghai 200011, China.
*Corresponding author. Email: xudongwang70@hotmail.com (X.W.); roritchie@lbl.gov (R.O.R); mpezwei@nus.edu.sg (W.Z.)

strong B—O—C covalent bonds with PVA nanolayers for mechanical strengthening (38, 39). Furthermore, MgB$_2$ nanosheets could provide conducting ions and electrons for enhanced electrical properties (40). Through this approach, we have successfully created hierarchical lamellar MgB$_2$ nanosheet (HLMN)–bridging PVA hydrogels, exhibiting impressive tensile strength (8.58 to 32.7 MPa) and toughness (27.56 to 123.3 MJ/m^3). In addition, these nanocomposite hydrogels demonstrate high sensitivity to deformation pressure, characterized by a remarkable response/relaxation time of 20 ms and a detection lower limit as low as 1 Pa. These remarkable properties make them suitable for a wide range of applications across various fields.

RESULTS AND DISCUSSION

The fabrication process of the HLMN-hydrogel begins with the synthesis of 2D MgB$_2$ nanosheets using a chemical exfoliation method based on chelation reactions. Figure 1A shows the crystal structure of MgB$_2$, highlighting its layered characteristics consisting of distinct and alternating Mg and B layers. This layered configuration is further confirmed by the scanning electron microscopy (SEM) image (fig. S1) of a micro-MgB$_2$ particle, which reveals a plate-like structure with a pronounced length-to-thickness ratio. This layered structure of MgB$_2$ presents the potential for its exfoliation into nano-sized, 2D nanosheets. However, the crystal bonding within MgB$_2$ is complex and strong. Specifically, MgB$_2$ exhibits an AlB$_2$-type crystal structure, consisting of closely packed Mg layers and graphene-like B layers bonded by a combination of ionic interlayer bonding and a mixture of covalent and metallic bonding (41). To overcome the formidable crystal bonding and successfully exfoliate MgB$_2$ nanosheets, we use chelation reactions, through which a metal ion forms a strong complex with an organic ligand, thereby extracting the metal ion from its original position (42). EDTA, chosen as the chelating agent, has four
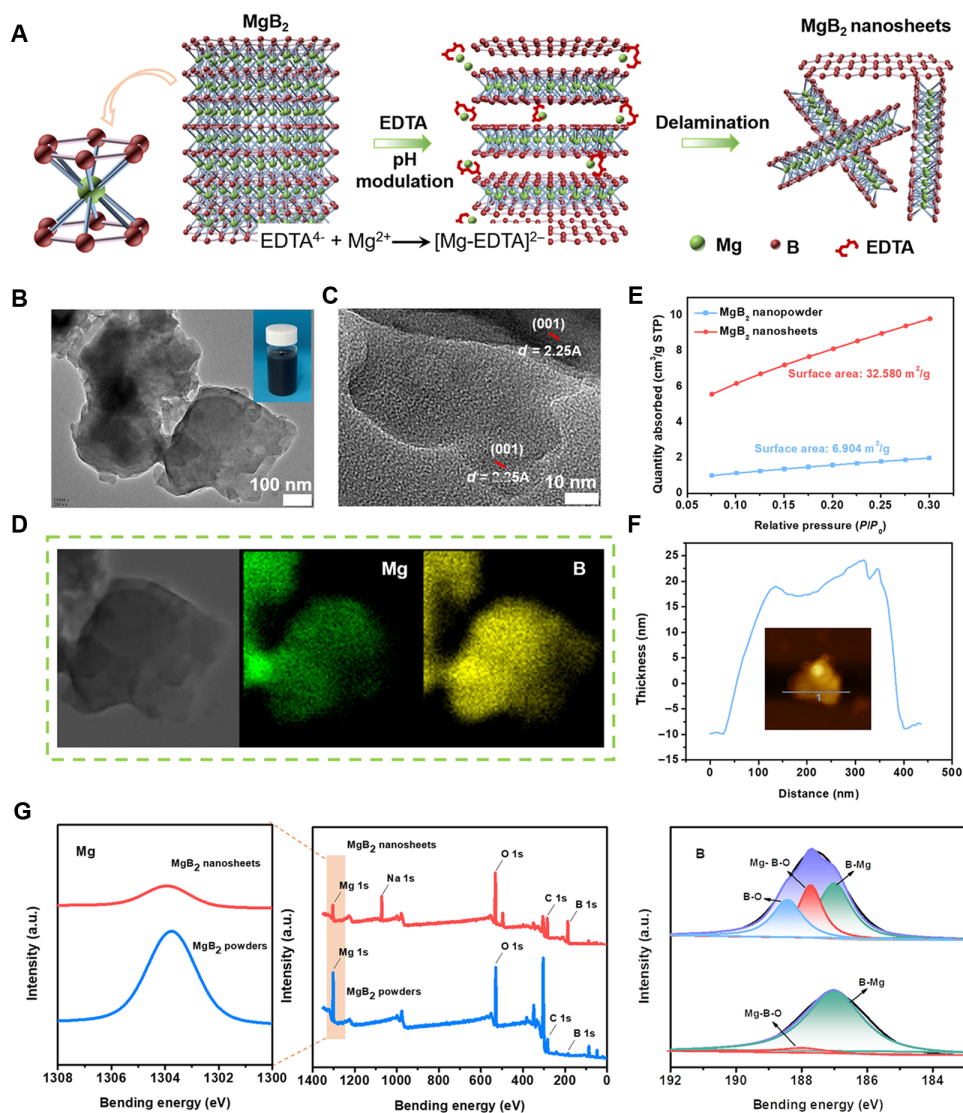

Fig. 1. Fabrication and characterizations of the MgB₂ nanosheets. (**A**) Schematic illustration of the exfoliation process for MgB$_2$ nanosheets. (**B** and **C**) TEM and HRTEM images of exfoliated MgB$_2$ nanosheets. (**D**) TEM-EDS of the MgB$_2$ nanosheets. (**E**) Surface area of the MgB$_2$ nanosheets. (**F**) AFM image of the nanosheets. (**G**) XPS of MgB$_2$ nanosheets.

acidic protons enabling the formation of strong Mg-EDTA complexes, as displayed in fig. S2. When MgB_2 nanoparticles react with EDTA, EDTA firmly engages with the Mg, extracting them from their native positions within the crystal structure. This interaction leads to a Mg-deficient layered structure, which weakens the interlayer bonding within the MgB_2 crystals and facilitates their cleavage into MgB_2 nanosheets under the influence of ultrasound vibrations. The resultant exfoliated MgB_2 nanosheets exhibit a thin-plate microstructure approximately 500 nm in length and 20 nm thick, as confirmed by the transmission electron microscope (TEM) image and atomic force microscopy (AFM) data in Fig. 1 (B, C, and F, respectively). This result verifies the successful exfoliation into 2D MgB_2 nanosheets. Furthermore, Brunauer-Emmett-Teller (BET) surface area analysis measurements reveal a significant increase in surface area from 6.904 m^2/g for the MgB_2 nanoparticles to 31.580 m^2/g for the MgB_2 nanosheets (Fig. 1E). Energy-dispersive spectroscopy analysis under TEM (TEM-EDS) confirms the composition of Mg and B elements in the MgB_2 nanosheets (Fig. 1D). X-ray photoelectron spectroscopy (XPS) is used to demonstrate the reduction of the Mg element in the MgB_2 nanosheets (Fig. 1E). A clear distinction is observed in the B1s XPS spectra between the MgB_2 nanoparticles and nanosheets. In the MgB_2 nanosheets, the B1s peak splits into three distinct peaks at approximately 187, 187.7, and 188.4 eV (Fig. 1G). The broader peak observed at 188.4 eV in the MgB_2 nanosheets can be attributed to an increased presence of B—OH species (43). With this change in dimension and increased boron composition, these MgB_2 nanosheets show great promise for enhancing the mechanical and electrical performances of conductive PVA hydrogels.

The HLMN-hydrogel was then prepared by a combination of evaporation-driven self-assembly and bridging–cross-linking approach, as shown in Fig. 2A. This process starts by blending 0.16 wt % MgB_2 nanosheets with 4 wt % PVA aqueous solutions, which is the highest ratio of MgB_2 nanosheets that can be added without affecting the fluidity of the mixture. As shown in fig. S4, when the PVA content is increased to 8 wt % or the MgB_2 nanosheets content is raised to 0.24 wt %, the mixture undergoes a swift transition from a liquid state to a gel-like consistency, thereby hindering the self-assembly process. This change also indicates an effective boronate-ester bonding creation between the B—OH species of the MgB_2 nanosheets and the hydroxyl groups (-OH) of the PVA. This flowable mixture then undergoes an evaporation process in an ambient environment to form either a thin film or a bulk shape, depending on the duration of evaporation. During the evaporation process, dehydration reactions occur among the hydroxyl groups of PVA, leading to the layer-by-layer assembly of PVA micro/nanolayers bonded by hydrogen bonds. Meanwhile, leveraging their high aspect ratio, the MgB_2 nanosheets naturally align with their flat surfaces parallel to the PVA layers, facilitating the formation of boronate-ester bonds in between. This process forms the initial cross-linking of the composite system assisted by the hydrogen bonds and boronate-ester bonds. Subsequently, the sample undergoes a low-temperature thermal annealing, which largely increases the number of PVA nanocrystalline domains within the PVA layers and the formation of boronate-ester bonds bridging the MgB_2 nanosheets with the PVA layers, as illustrated in Fig. 1A. Last, the annealed sample is swelled in water until equilibrium to achieve the HLMN-hydrogel, which consists of ~93% water content, as confirmed in fig. S5.

For comparison, we also prepared pure PVA hydrogels (PVA-hydrogel) and MgB_2 nanoparticle–doped PVA hydrogels (MP-hydrogel) using similar evaporation-assisted self-assembly and thermal annealing methods. The microstructures of these comparing samples are examined in fig. S6. The PVA hydrogels display a well-ordered lamellar microstructure due to the evaporation-driven self-assembly effect. However, the MP-hydrogels exhibit a less orderly structure due to the spherical shape of the MgB_2 nanoparticles (fig. S7) that disrupts the orderly formation of PVA layers during evaporation. The HLMN-hydrogels, however, showcase a perfectly aligned lamellar microstructure, owing to the 2D platelet–like shape of the MgB_2 nanosheets. These nanosheets, with their high aspect ratio and nanometer thickness, fit perfectly between the PVA layers. The formation of boronate-ester bonds further strengthens the connections between the PVA layers and the MgB_2 nanosheets, promoting a refined layer-by-layer assembly of the materials during the evaporation process. The SEM images (Fig. 2B) highlight the hierarchical lamellar microstructure of the HLMN-hydrogel, with nanoscale alternating PVA layers and MgB_2 nanosheet layers. Specifically, the nanocomposite hydrogel consists of the following hierarchical lamellar structures and multiple molecular bonds: (i) Through the evaporation process, PVA chains assemble into nano- and microscale lamellar layers with MgB_2 nanosheets embedded in-between; (ii) the PVA layers, interconnected via hydrogen bonds, comprise numerous nanocrystalline domains formed during thermal annealing; (iii) MgB_2 nanosheets serve as high-functionality crosslinks, producing an abundance of boronate-ester bonds through the interaction of B—OH species on the MgB_2 nanosheets and the -OH groups of the PVA layers.

Uniaxial tensile tests were conducted on all samples, with results presented in Fig. 2C. The HLMN-hydrogel, despite consisting of a high-water content of ~93%, displayed substantially superior mechanical properties compared to the other groups. Its tensile strength (8.58 ± 1.34 MPa) was 11 times higher than that of the PVA-hydrogel (0.78 ± 0.04 MPa) and 2.7 times that of the MP-hydrogel (3.17 ± 0.56 MPa) (Fig. 2, C and D). The toughness of the HLMN-hydrogel, measured as the area under the stress-strain curve, further showcased its superiority. The value for the HLMN-hydrogel (27.56 ± 7.48 MJ/m^3) was nearly 20 times larger than the PVA-hydrogel (1.37 ± 0.21 MJ/m^3) and 3.7 times larger than the MP-hydrogel (7.45 ± 1.88 MJ/m^3). By modulating the water contents, the mechanical performance of the HLMN-hydrogels could be further enhanced (fig. S10). The mechanical properties of the HLMN-hydrogel exceeded that of most hydrogels (Fig. 2F and table S1). Furthermore, the HLMN-hydrogel displayed a great shape recovery capability and decent hysteresis performance (Fig. 2E). These results demonstrate the advantages of our facile assembly approach for fabricating strong and tough hydrogels.

The remarkable strength and toughness of HLMN-hydrogel, capable of supporting a 2 kg load with a thin strand (0.3 mm by 3 mm), can be attributed to the synergistic energy dissipation mechanisms from their hierarchical lamellar structures and multiple molecular bonds, as illustrated in Fig. 3A. On a micro- and nanoscale, the well aligned MgB_2 nanosheets embedded within the PVA layers (Fig. 3A) impede crack propagation via fracture deflection. Simultaneously, the pullout of MgB_2 nanosheets from the PVA layers dissipates additional mechanical energy and enhances the overall deformation capability, allowing the HLMN-hydrogel to stretch more than 10-fold its original length. This is over three times the stretchability of pure PVA-hydrogels, which can only reach thrice their original length before fracturing (Fig. 2D). SEM images of cross-sectional
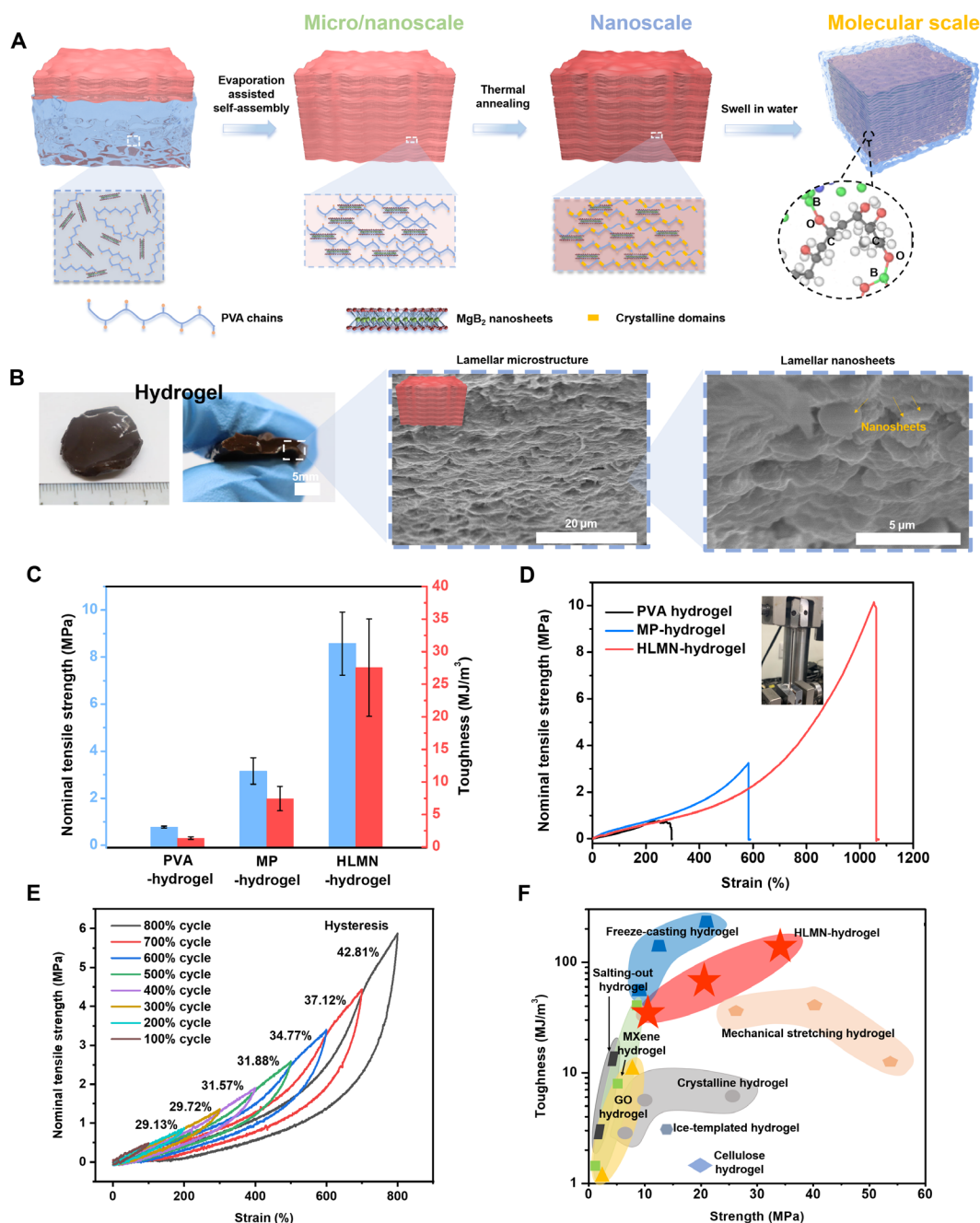
Fig. 2. Fabrication and mechanical performance of the HLMN-hydrogel. (**A**) The hierarchical design strategy ranging from molecular to macro scale via self-assembly and boron bridging. (**B**) Morphology of the HLMN-hydrogel. SEM images revealing the lamellar micro/nanostructure of the HLMN-hydrogel. (**C**) Strength and toughness of the PVA hydrogel, MP-hydrogel, and HLMN-hydrogel. (**D**) Engineering stress-strain curves of the four kinds of hydrogels. (**E**) Cyclic loading-unloading of one HLMN-hydrogel and its hysteresis performance. (**F**) A plot of the toughness versus strength of HLMN-hydrogel and other tough hydrogels. The data are summarized in table S1. The data reported in (B) represent the mean value, with the error given as the standard deviation. The sample size is 5 for all of the cases.

fractures corroborate this, revealing a deflected fracture surface across multiple layers and the identifiable pullout of individual MgB$_2$ nanosheets (Fig. 3, C and D). At the nanoscale, the PVA layers were reinforced by thermal annealing to form abundant nanocrystalline domains, which consist of highly aggregated and intertwined PVA chains with strong molecular bonding. The fracture of these highly crystallized PVA layers lead to significantly energy dissipation.

Differential scanning calorimetry (DSC) analysis (Fig. 3F) reveals a broad curve for annealed HLMN-hydrogels with higher intensity compared to unannealed ones. This suggests the formation of more crystalline domains in the annealed HLMN-hydrogels. The highly crystallized anisotropic lamellar microstructure of the HLMN-hydrogel can also be identified by the flattened circular and elliptical-like pattern from the small-angle x-ray scattering (SAXS) tests
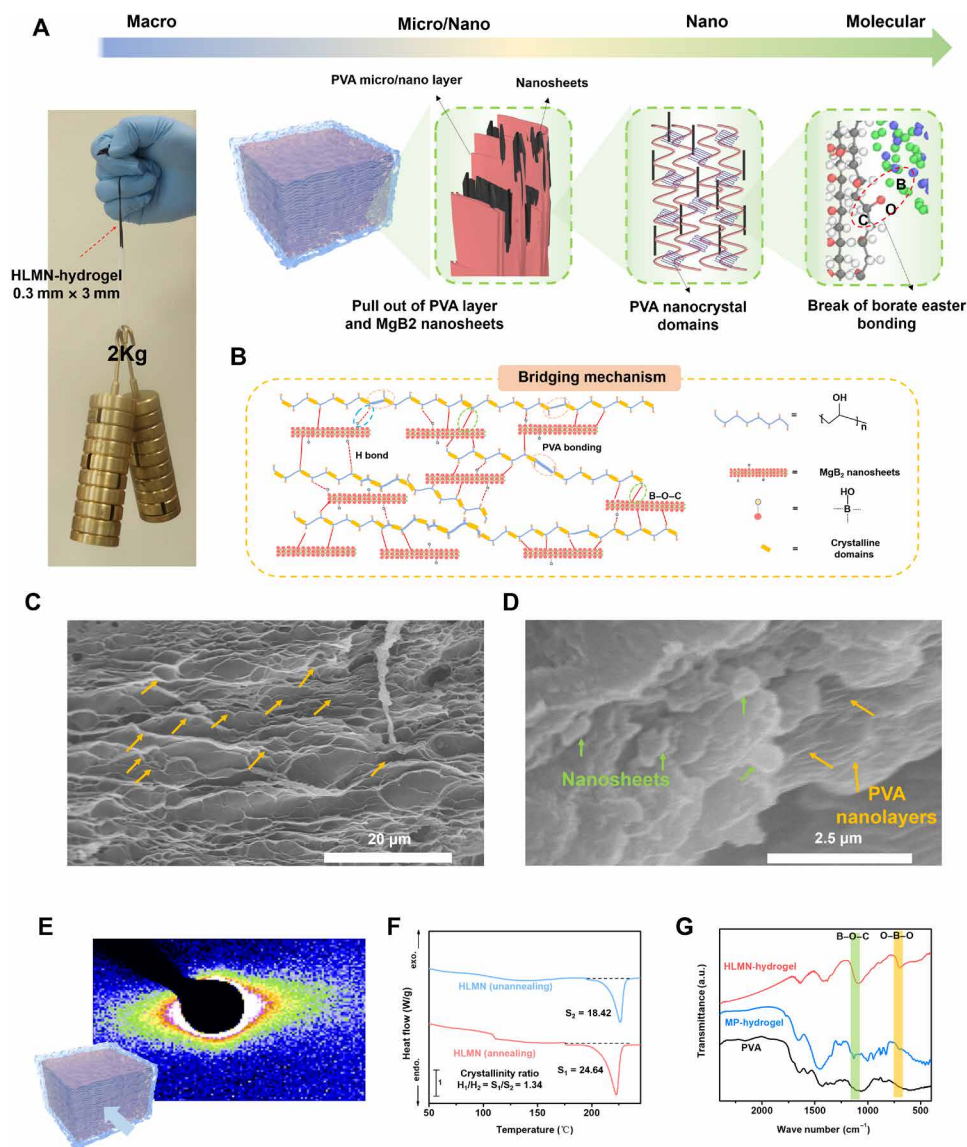
Fig. 3. Toughening mechanisms of hierarchical lamellar design and boron bridging cross-linking. (**A**) Hierarchical strengthening mechanism of the HLMN-hydrogel during fracture. (**B**) Bridging mechanism between MgB$_2$ nanosheets and PVA chains in the molecular scale (green circle, B—O—C bond; blue circle, H bond; yellow circle, PVA bonding). (**C**) Cross-sectional microstructure of the HLMN-hydrogel. Yellow arrows indicated the fracture of hierarchical layers. (**D**) Pull-out of nanosheets (green arrows) and PVA nanolayers (yellow arrows) from the hydrogel. (**E**) SAXS patterns of the HLMN-hydrogel. (**F**) Crystalline domains analysis via DSC. (**G**) FTIR of three kinds of hydrogels.

(Fig. 3E). An enormous number of boronate-ester bonds were formed to bridge the MgB$_2$ nanosheets and the PVA layers at molecular scale, augmenting the strength and toughness of the hydrogels as high-functionality cross-links. The existence of B—OH species on the surface of the MgB$_2$ nanosheets was confirmed from the XPS results in Fig. 1G. The appearance of the B—O—C bonds (1125 cm^{-1}) and O—B—O bonds (710 cm^{-1}) (38, 44, 45) in the Fourier transform infrared spectroscopy (FTIR) results of HLMN-hydrogels confirmed the creation of strong covalent boronate-ester (B—O—C) bonds in between the MgB$_2$ nanosheets and PVA layers (Fig. 3G). During stretching, debonding of these B—O—C covalent bonds consumes a significant amount of energy that leads to high strength and toughness of the hydrogels. In summary, the HLMN-hydrogel's outstanding

mechanical performance is a result of a synergic effect of multiple energy dissipation mechanisms, including crack deflection by the MgB$_2$ nanosheets, the pulling-out of the MgB$_2$ nanosheets from the PVA layers, the fracture of the highly crystallized PVA layers, and the debonding of the strong B—O—C covalent bonds in between the MgB$_2$ nanosheets and PVA layers.

The HLMN-hydrogel not only exhibits outstanding mechanical performance but also exceptional response sensitivity and low detection limit. Specifically, the pressure sensor can respond to a slight pressure of ~1 Pa, equivalent to a small flower weighing 56 mg on an area of 5 cm^2 (Fig. 4A). The response/relaxation time of HLMN-hydrogel is remarkably low at ~20 ms, even faster than that of human skin (≈30 to 50 ms) (46) and electronic skin (table S2). In

addition, the gauge factor (GF) of the HLMN-hydrogel increases from 0 to 4.43 as the stretch strain increases from 0 to 800% (Fig. 4B). In contrast, control studies of the MP-hydrogel showed a poorer response time, relaxation time, and GF compared to the HLMN-hydrogel (fig. S13). The electrical stability of the HLMN-hydrogel is retained after 1500 tensile cycles, indicating its potential as a robust mechanical sensor (Fig. 4C).

The HLMN-hydrogel displays electrical conductivity by facilitating the movement of both electrons (through MgB_2 nanosheets) and ions (such as Mg^{2+} and B species). The presence of conducting ions was confirmed through inductively coupled plasma emission spectrometer (ICP) analysis of the hydrogels (fig. S15). In a

temperature-resistance experiment (fig. S17), the resistance of the hydrogel decreased with the increase in temperature, indicating an increased movement of ions due to the elevated temperature, and further validating the existence of the ionic conducting mechanism of the HLMN-hydrogel. We further conducted a comprehensive electrochemistry study to analyze the conductive format and calculate conductivity. From the results shown in fig. S18, it is evident that the ion resistance measures at 9.93 ohms, while the electron resistance is notably high. This observation indicates the dominance of ion resistance, which aligns with expectations, considering the coverage of nanosheets by the PVA, affecting their electronic conductivity. Further insight from the Bode plot in fig. S18C reveals an
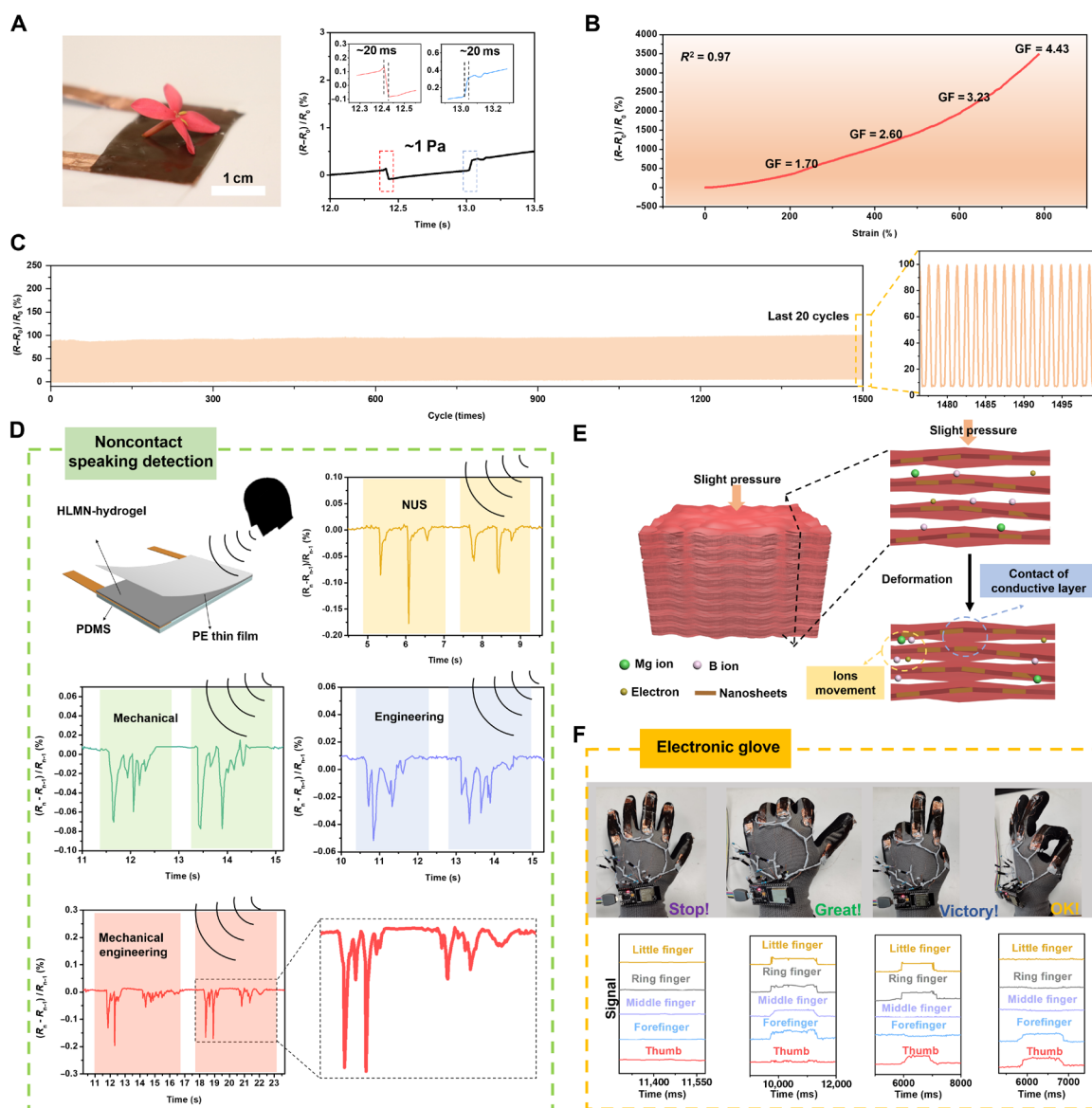

Fig. 4. Sensing capabilities and applications of the conductive HLMN-hydrogel. (**A**) Photo image and electrical response of a conductive HLMN-hydrogel sensor weighted by a small flower. The pressure applied on the hydrogel by the flower is ≈1 Pa. The response/relaxation time is 20 ms. (**B**) GF of the HLMN-hydrogel. (**C**) Cycle stability of the HLMN-hydrogel. (**D**) Noncontact speaking detection using the HLMN-hydrogel. The detection device showed different and unique signals when they "sounded" different words. (**E**) Schematic illustration of the mechanism of the outstanding detection capability. (**F**) Electronic-glove fabrication using HLMN-hydrogel. Photos showing different hand gestures with E-glove and the associated signal responses from five fingers.

exceptionally low deviation frequency for ionic conduction in the material. These outcomes reaffirm that ionic transport is the predominant factor in the hydrogel's behavior. Our calculations yielded a material conductivity of 0.13 S/m. We compared this conductivity with that of several other conductive hydrogels and composites in table S3 and observed that its value is not exceptionally high. However, it is essential to emphasize that our objective does not prioritize achieving high conductivity. This is because high conductivity alone does not necessarily correlate with improved sensing performance.

The exceptional sensing ability of the HLMN-hydrogel is due to its ordered nanoscale lamellar conductive PVA-MgB$_2$ layers and extremely low compressive modulus (1.86 ± 0.10 kPa), as shown in fig. S19. The HLMN-hydrogel's low compressive modulus allows for noticeable nanoscale deformation even under minimal force. This leads to a reduction in layer gaps that accelerates the transportation of Mg^{2+}, B species ions, and electrons for enhanced conductivity (Fig. 4E). Significantly, the nanoscale lamellar microstructures lead to a significant increase in contact areas between the multiple conductive PVA-MgB$_2$ nanolayers, creating a more efficient conducting path for electrons and ions. This change in contact area is particularly noticeable and can persist until the pressure is removed (Fig. 4A).

Notably and interestingly, our HLMN-hydrogel demonstrated remarkable noncontact speaking sensing ability due to its exceptional response sensitivity and low detection limit (Fig. 4D and movie S1). The HLMN-hydrogel produced stable and distinguishable signals when receiving spoken words such as "NUS," "mechanical," and "engineering." The signal for mechanical engineering represented the combined signal of "mechanical" and "engineering," demonstrating the accuracy and stability of the HLMN-hydrogel (Fig. 4D). In addition, the HLMN-hydrogel also exhibited great underwater speaking sensing capability, as depicted in fig. S21. We spoke the words "Mechanical" and "Engineering" to the hydrogel while it was immersed in water. Each word was repeated twice to confirm its accuracy. The signal corresponding to "Mechanical" is presented in fig. S21B. After applying Fourier transformation, it becomes evident that the signals for the two instances of "Mechanical" exhibit similar characteristic frequencies, which distinctly differ from the signals for "Engineering" (fig. S21, C, D, F, and G). This underscores the hydrogel's exceptional sensing capacity even when submerged in water. Moreover, by using the five output channels, the HLMN-hydrogel can be fabricated into an electronic glove to distinguish different unique signs, including "stop," "great," "victory," and "ok" (Fig. 4F). In addition, the HLMN-hydrogel can act as a handwriting-sensing device, detecting distinguishable and highly repeatable waveforms for the words "ME" and "OK" (fig. S23). These experiments demonstrate the superior sensing capabilities and versatile applications of the HLMN-hydrogel.

The HLMN-hydrogel and its device, with outstanding sensing capability, displayed tremendous potential for consumer electronics, including speaking detection, virtual recreational gaming, sign language translation, remote control of the surgical robot, rehabilitation tool for patients with hand disease, etc. For noncontact speaking detection, we displayed a simple application example. The signals of verbal instructions, such as "blue," "red," "yellow," "green," and "turn off" were received by the HLMN-hydrogel. The collected quantities of signals were used for the training of a neural network algorithm self-built using Python (fig. S24). Afterward, the speaking and commands transfer was achieved by a microcontroller (Fig. 5A).

Different verbal instructions of "blue," "red," "yellow," "green," and "turn off" exhibited accurate corresponding commands of turning up the blue, red, yellow, or green light-emitting diode (LED) lights and turning off the lights (Fig. 5B and movie S2). In addition, Fig. 5C showcased another application formats. A robotic car executed the instructions to pick up and transport the "tomato," "orange," "plum," and "grape," as the hydrogel received the spoken commands for "tomato," "orange," "plum," and "grape" (movie S3). Accordingly, it is apparent that the fabricated hydrogels with the noncontact speaking sensing capabilities can realize the ability to "listen" and to "understand" by themselves. The results showed that HLMN-hydrogel has high sensitivity, accuracy, stability, and great potential as sensors and consumer electronics.

Furthermore, in anticipation of future applications of this sensing hydrogel in the biomedical field, we carried out an extensive assessment of the biocompatibility of the hydrogel, encompassing both in vitro and in vivo studies. To initially assess the biocompatibility of the hydrogel, we performed a hemolysis assay. As depicted in Fig. 6 (A and B), the suspension of red blood cells (BCs) treated with the hydrogel appeared colorless and clear, with an almost negligible hemolysis ratio when compared to Triton X-100. This observation signifies the excellent blood compatibility and overall biosafety of the hydrogel. Next, we cultured rat skin–derived 1 (RS1) fibroblast cells with the hydrogel for 48 hours, followed by a live/dead staining procedure to assess the cells' growth status (Fig. 6C). Our observations revealed robust cell growth and almost no cell death even after 48 hours of culture with the hydrogel. Furthermore, we performed a quantitative analysis using the cell counting kit-8 (CCK-8) assay on the RS1 cells after 48 and 72 hours of culture with the hydrogel (Fig. 6D). The results demonstrated a consistent increase in cell viability over time, and the proliferation capacity of the hydrogel sample closely resembled that of the blank culture plate. These findings underscore the excellent cell biocompatibility of the hydrogel. Last, to assess the in vivo biosafety of the hydrogel, it was surgically implanted into bilateral pockets within the perivertebral fascia lumbodorsalis of Sprague-Dawley (SD) rats under anesthesia. After 2 weeks, the optical images revealed no signs of tissue swelling or inflammation in the implanted area (Fig. 6E). Histological analysis was performed on subcutaneous tissue and vital organs, including the heart, liver, spleen, lung, and kidney, using hematoxylin and eosin (H&E) staining (Fig. 6, E and F). No discernible differences were observed between the tissues of the blank and hydrogel samples. Furthermore, there were no notable abnormalities in cell morphology and no signs of neutrophil or lymphocyte infiltration or the presence of necrotic cells in these tissues. These findings indicate the good biocompatibility and safety of the HLMN-hydrogel.

If MgB$_2$ nanosheets were to be replaced with a different type of nanosheet while maintaining the same assembly method, the nanosheets and PVA nanolayers would still be present based on the fabrication mechanism analysis. However, the crucial molecular-level interaction between the nanosheets and the polymer matrix would cease to exist, resulting in a decline in mechanical performance. What sets MgB$_2$ nanosheets apart from other nanosheets is their ability to establish cross-links with the PVA matrix through the formation of B—O—C bonds, thereby fortifying and toughening the matrix. Typically, such cross-linking processes happen rapidly, resulting in PVA gelation, which can affect the assembly and alignment of nanosheets within the polymer matrix. In our study, we harnessed the self-assembly–induced bridge cross-linking approach,
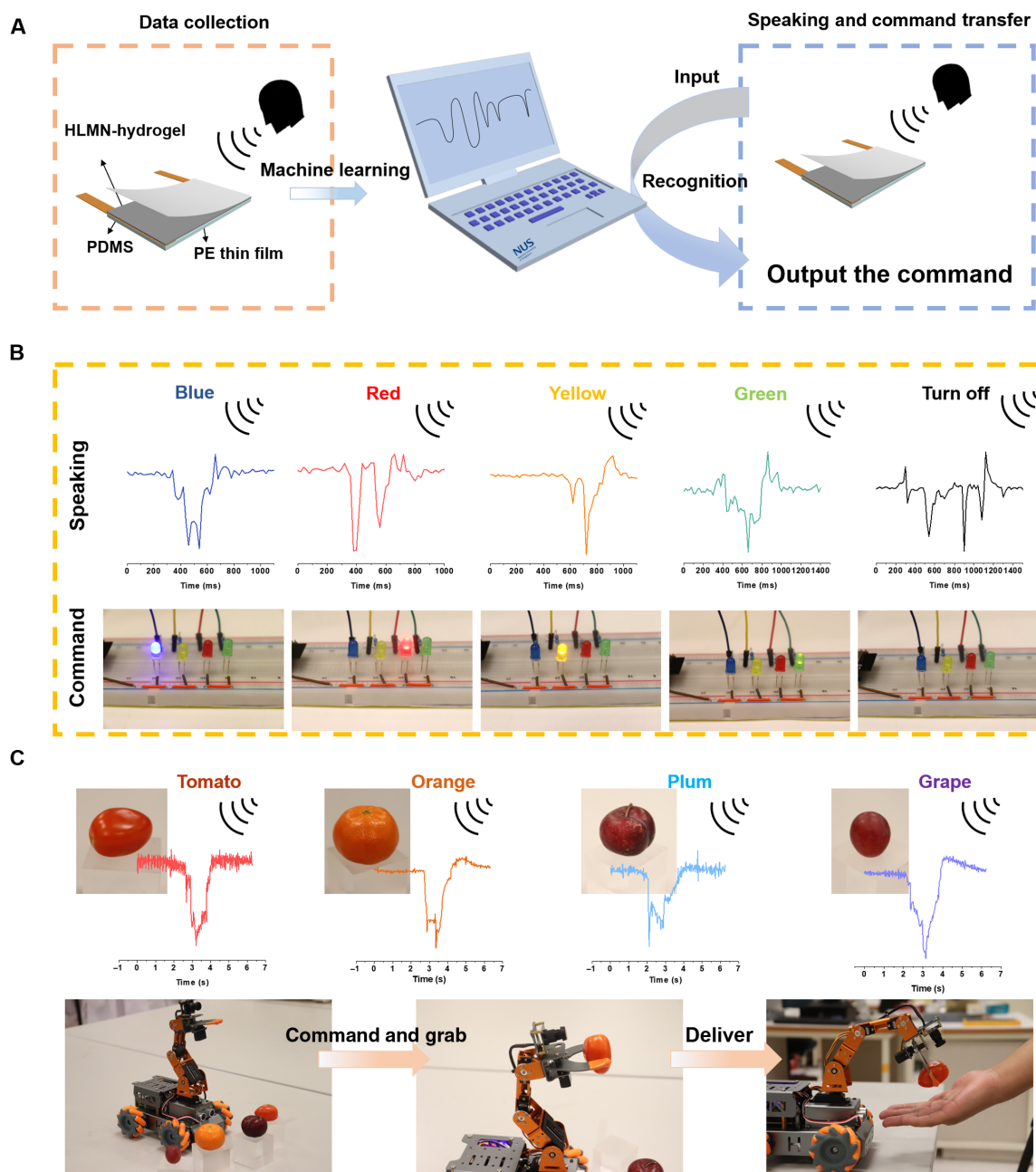
Fig. 5. Speaking and commands recognition of the conductive HLMN-hydrogel. (**A**) Scheme showing the speaking and commands recognition procedure. (**B**) The LED light performed the commands of turning up blue, red, yellow, green light or turning off the light, when hydrogel received the verbal instructions of "blue," "red," "yellow," "green," and "turn off." (**C**) Robot performed the commands of pick up and deliver the tomato, orange, plum and grape, when hydrogel received the verbal instructions of "tomato," "orange," "plum," and "grape."

allowing the combination of MgB_2 nanosheets with PVA and the alignment of MgB_2 nanosheets within PVA layers to coincide with water evaporation. This method overcomes the limitations associated with traditional "top-down" engineering techniques, which often face challenges in establishing strong bonds between hierarchical units after the gelation process.

Regarding sensitivity, if MgB_2 nanosheets were replaced with other types of nanosheets, it is very likely that the hydrogel's sensitivity would remain intact. This is because the presence of nanoscale layers,

a key factor contributing to high sensitivity to external pressure, would persist. Therefore, fabricating a highly sensitive hydrogel using this method with different nanosheets remains a viable approach. However, achieving a hydrogel with the same level of strength and toughness as demonstrated in this study may not be feasible. Certainly, by modifying the nanosheets with specific functional groups and incorporating these modified nanosheets into the hydrogel system, it is possible to establish cross-links between the inorganic nanosheets and the polymer matrix. This approach can yield a conductive hydrogel with
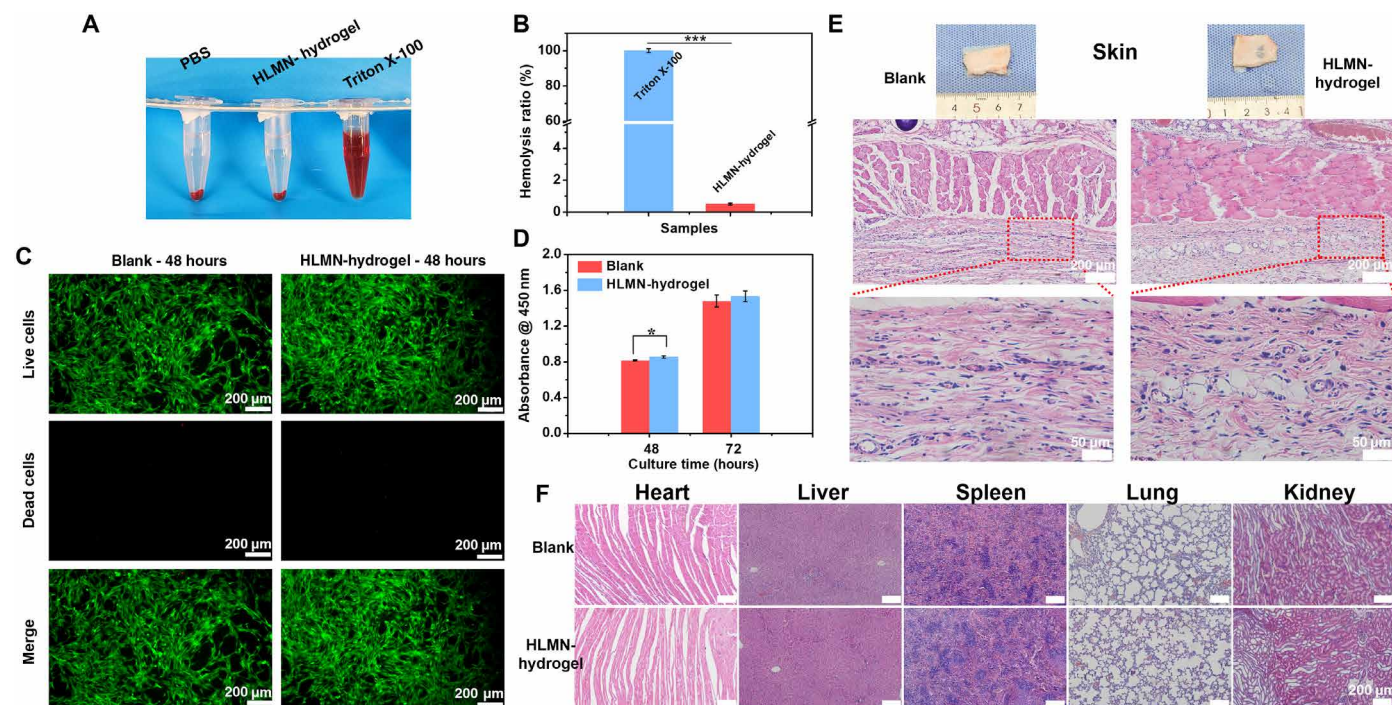
Fig. 6. Biocompatibility study of the HLMN-hydrogel. (**A**) Hemolytic test to assess the blood compatibility of the hydrogel in vitro. (**B**) Quantitative analysis of the hemolysis ratios ($n = 5$, ***$P < 0.001$). (**C**) Culture of RS1 cells with hydrogel to assess cell biocompatibility using a live/dead dye assay. (**D**) Quantitative analysis the cell growth after 48 and 72 hours of culture ($n \geq 3$, *$P < 0.05$). (**E**) Implant the hydrogel into bilateral pockets within the perivertebral fascia lumbodorsalis to assess the in vivo biocompatibility of the hydrogel. Optical image and histological analysis of subcutaneous tissue following 2-week hydrogel implantation with H&E staining. (**F**) Histological analyses of the rat organs (heart, liver, spleen, lung, and kidney) with hydrogel implantation and without.

exceptional mechanical performance and sensitivity. This research sets the foundation for developing a series of robust, resilient, and sensitive conductive hydrogels through hierarchical structural design spanning from the micro to molecular scales.

In summary, we have introduced an electrically conductive hydrogel, which uses MgB_2 nanosheets to bridge a unique hierarchical lamellar structure of PVA nanocomposite hydrogels. The resulting HLMN-hydrogel exhibits exceptional mechanical properties, including strength (8.58 to 32.7 MPa) and toughness (27.56 to 123.3 MJ/m^3), as well as remarkable sensing capabilities with a reaction time of 20 ms and a detection lower limit of ~1 Pa. By incorporating hierarchical lamellar layers and interface cross-linking bridges, the mechanical performance of HLMN-hydrogel exceeds that of recently reported tough hydrogels. Moreover, the HLMN-hydrogel demonstrates exceptional noncontact speaking sensing ability due to its unique nanoscale layered structure, enabling accurate and stable detection of verbal commands. These features make the HLMN-hydrogel an attractive material for flexible electronics, e-skins, soft robotics, energy, and biomedical applications. Overall, our hierarchical design strategy provides an effective approach for developing robust and functional hydrogels with advanced capabilities.

MATERIALS AND METHODS
Materials
PVA (99+% hydrolyzed, M_w 89,000 to 98,000), NaOH, and EDTA were purchased from Sigma-Aldrich. MgB_2 powder was brought from Xiaohuang Nanotech, Shanghai.

Synthesis of MgB₂ nanosheets
The reaction solution was obtained by adding EDTA (12.89 g) and NaOH (3.95 g) into 90 ml of H_2O. Then, the pH of the reaction solution was adjusted to 10. MgB_2 powder (2 g) exfoliation happened when added to the reaction solution (25°C). After 3 days of exfoliation, the suspension was washed at least five times using deionized water and centrifuged to separate the powders. The collected precipitation was dispersed in water and delaminated under probe sonication for 30 min. After that, the dispersion was centrifuged for 10 min at 10,000 rpm, followed by freeze-drying and annealing at 750°C to obtain MgB_2 nanosheets.

Fabrication of the HLMN-hydrogel, PVA hydrogel, and MP-hydrogel
First, the fabricated MgB_2 nanosheets were ultrasonic dispersed in water with a pH of 9. PVA solution (4 wt %) was obtained after adding PVA into the mixture in a 90°C water bath for 1 hour, with a weight ratio of the MgB_2 nanosheets and PVA of 4%. The mixed solution was then poured into a container for evaporation-assisted self-assembly. The obtained lamellar dry gel was then thermally annealed at 60°C for 30 min to produce PVA crystalline domains and cross-linking bridges. The HLMN-hydrogel was obtained by soaking the annealed gel in deionized water till equilibrium. To prepare the PVA hydrogel, a 4 wt % PVA solution was subjected to evaporation-assisted self-assembly and low-temperature annealing at 60°C, followed by soaking in water until equilibrium. For the MP-hydrogel, MgB_2 powders passing through the 400-mesh screen were mixed with PVA solution, with the same self-assembling, annealing, and swelling process carried out.

Characterization

The microstructure and element mapping of MgB_2 nanosheets were characterized on a TEM (JEM-2100F, Japan). XPS (ESCAlab250 Thermal Scientific, USA) was used to determine the element composition of the materials, while x-ray diffraction (D8 Advance, Bruker) was used to determine the phase of the materials. The microstructural images of the hydrogel were obtained by an SEM (HITACHI S-4800). The hydrogel samples for microstructure observation were first freeze-dried and then were frozen in liquid nitrogen for cross section preparation. The bonding of the hydrogel was analyzed by FTIR (Thermal Scientific, USA). The thickness and size of nanosheets were analyzed by AFM (Park NX20). BET surface areas were obtained via Quantachrome Autosorb. SAXS measurements were performed on a Xenocs Xeuss 2.0 system by placing the cross section of the hydrogel perpendicular to the x-ray beam. The water contents of the HLMN-hydrogel were estimated by comparing the mass difference between the samples in the water-containing state and dried state.

DSC measurement

DSC was used to test crystalline domains at a rate of 20°C/min under an argon atmosphere with a flow rate of 50 ml/min. Before testing, hydrogel slices were first immersed in a cross-linking agent (50 vol % glutaraldehyde, 5 ml; 37 wt % hydrochloric acid, 500 μl; water, 50 ml) to stabilize the amorphous chains. Then, excess hydrochloric acid was washed out from the stabilized hydrogels for 2 hours before they were dried in a 50°C blast oven overnight.

ICP test

The ion concentration in the reaction mixture was tested using ICP. First, MgB_2 nanosheets were ultrasonic dispersed in alkaline water (pH 9) for 10 min. Then, the dispersed solution was magnetic stirred for 1 hour in a 90°C water bath. Last, the supernatant was collected after centrifugation for the ICP test. In the stability test, the ion concentration in the water solution (20 ml) after soaking the dry hydrogel (0.5 g) for 3 and 7 days was also investigated using ICP.

Mechanical performance

The mechanical performance of the hydrogels was evaluated using a universal tensile machine (Instron 5500) equipped with a maximum force of 1000-N loading cell. Dog bone–shaped hydrogel samples (width, 3 mm; length, 8 mm; thickness, 0.2 mm) were cut using a die cutter and uniaxially tested in tension at a displacement speed of 20 mm/min. The toughness of the hydrogels was determined by calculating the area under the stress-strain curve. At least five samples were tested for each type of hydrogel. The fracture energy (Γ) of the samples was obtained by single-edge notch tension (SENT) test and calculated through the following equation

$$\Gamma = \frac{6Wc}{\sqrt{1 + \varepsilon_0}} \tag{1}$$

where ε_0 represents the fracture strain of notched sample, c is the length of the notch, and W is the stretch energy calculated by integration of the nominal tensile strength versus strain of an unnotched specimen with the same dimensions stretched to the ε_0 strain. The hysteresis performance of the materials is determined using the calculation: Hysteresis $= (S_L - S_U)/S_L \times 100\%$, with S_L and S_U representing the areas under the loading and unloading curves at a specific strain, respectively (20, 47).

Conductivity study

We performed an electrochemical study to investigate the material's conductivity using an electrochemical workstation (VMP3, Biologic Inc.). To examine the conductive behavior of the material, we developed an equivalent circuit model that incorporates both ionic and electronic components (48). In the analysis of ionic conduction, we used the Randle equivalent circuit (49), with R_i representing ionic resistance and C_{dl} representing double-layer capacitance. Parallel to the double-layer capacitance, we considered the diffusion impedance due to the faradaic reaction, consisting of the charge transfer resistance R_{ct} and the Warburg impedance Z_w (the expression is illustrated in fig. S18A, where A_w is the Warburg coefficient, j is the imaginary unit, and ω is the angular frequency). The electronic-conducting component was represented by pure resistance, R_e. We treated ionic conductivity and electronic conductivity as independent, leading to R_e and ionic conductivity arranged in parallel (48). We determined the material's conductivity using the relationship between material size and conductivity: $\sigma = L/(SR)$, where L represents the electrode distance, S is the cross-sectional area of the material, and R is the resistance.

Self-healing

The HLMN-hydrogel was cut into two parts and then prehealed for 2 min. The prehealed samples were placed in an oven at 60°C for 5 min to promote the formation of bonds and crystalline domains at the crack. The healed hydrogel was obtained by swelling the samples in water.

HLMN-hydrogel for sensor applications

The reaction/relaxation time and GF of HLMN-hydrogel were explored using Keithley DMM6500 in the two-probe mode. For non-contact speaking detection, the hydrogel was encapsulated between polydimethylsiloxane (PDMS) film and polyethylene thin film (Fig. 4D). Two copper-pad electrodes were fixed on the PDMS film to ensure stable contact between hydrogels and Keithley DMM6500. A specialized algorithm $[r = (R_n - R_{n-1})/R_{n-1} \times 100\%]$ was used to mitigate the impact of water loss on resistance changes. For electronic glove application, the hydrogels were encapsulated with PDMS and attached to each finger joint of the glove. The end of the hydrogels was firmly attached to the glove by cyanoacrylate glue. The five hydrogel sensors were connected with the NodeMCU development board ESP-32S. For the handwriting sensor, the hydrogel was encapsulated into a dragon skin frame (fig. S23). A PDMS film was put on the hydrogel to protect it from mechanical failure during the writing.

HLMN-hydrogel for speaking and commands recognition

The collected speaking signals were processed in a self-built neuron network algorithm with Python. The speaking and commands transfer was achieved by a development board (NodeMCU, ESP-32S), which is compatible with the Arduino programming environment. All participants in the sensor application experiment were the authors of this manuscript, and the test was conducted with their informed consent.

Biocompatibility study in vitro and in vivo

To assess the blood compatibility of the hydrogel in vitro, a hemolytic test was used. Fresh BCs were sourced from SD rats procured from Shanghai Sippr-BK Laboratory Animal Co. Ltd. These BCs were subsequently subjected to centrifugation at 2000 rpm for 5 min. A 4% BC solution was prepared by mixing 0.2 ml of BCs with 4.8 ml of phosphate-buffered saline (PBS) solution. Hydrogels

were incubated in PBS for 24 hours to form the sample solution. Following this, 0.5 ml of the BC solution was combined with 0.5 ml of the sample solution, along with Triton X-100 and PBS, and the mixture was incubated at 37°C for 1 hour. Triton X-100 served as the positive control, while PBS served as the negative control. Subsequently, the supernatants were collected by centrifuging the samples at 2000 rpm for 5 min and were captured using a digital camera. Ultimately, the optical density (OD) of the supernatants was measured with a microplate reader at a wavelength of 540 nm. The hemolysis ratio of the hydrogel was calculated as follows: hemolysis ratio = $(OD_{hydrogel\ solution} - OD_{PBS})/(OD_{Triton\ X-100} - OD_{PBS}) \times 100\%$, where OD denotes the absorbance values of the hydrogel solution, PBS, and Triton X-100, respectively.

The cell compatibility in vitro of the hydrogel was assessed by culturing it with RS1 cells. RS1 cells were seeded with the density of 4×10^4 per well into 48-well plates with the hydrogel and were stained using live/dead dye (Calcein/propidium iodide cell viability/cytotoxicity assay kit, Beyotime) after a 48-hour culture to assess the cell status. In addition, RS1 cells were seeded into 48-well plates (8×10^3 cells per well) containing the hydrogels to evaluate cell viability. Subsequently, we conducted a quantitative analysis of RS1 cell viability using CCK-8 (Beyotime) after both 48 and 72 hours of culture.

To assess the in vivo biocompatibility of the hydrogel, the hydrogel was implanted into bilateral pockets within the perivertebral fascia lumbodorsalis of 8-week-old SD rats under anesthesia using pentobarbital sodium (0.5 mg/kg). Rats without any material implantation served as the control group. Subsequently, the animals were humanely euthanized through carbon dioxide (CO_2) asphyxiation after a 2-week period. Then, the histological analyses were conducted on the subcutaneous tissue surrounding the implanted hydrogel, as well as various rat organs, including the heart, liver, spleen, lung, and kidney using H&E staining. All the animal experiments were approved by the Institutional Animal Care and Use Committee of Shanghai Ninth People's Hospital Affiliated with Shanghai Jiaotong University, School of Medicine (SH9H-2023-A874-1).

Statistical analysis
All data were presented as the means ± standard deviation. The difference between two groups was analyzed using an unpaired Student's t test (*$P < 0.05$, ***$P < 0.001$).

Supplementary Materials
This PDF file includes:
Tables S1 to S3
Figs. S1 to S25
Legends for movies S1 to S3
References

Other Supplementary Material for this manuscript includes the following:
Movies S1 to S3

REFERENCES AND NOTES
1. W. Zhang, R. Wang, Z. Sun, X. Zhu, Q. Zhao, T. Zhang, A. Cholewinski, F. Yang, B. Zhao, R. Pinnaratip, P. K. Forooshani, B. P. Lee, Catechol-functionalized hydrogels: Biomimetic design, adhesion mechanism, and biomedical applications. *Chem. Soc. Rev.* **49**, 433–464 (2020).
2. Q. Hu, H. Li, E. Archibong, Q. Chen, H. Ruan, S. Ahn, E. Dukhovlinova, Y. Kang, D. Wen, G. Dotti, Z. Gu, Inhibition of post-surgery tumour recurrence via a hydrogel releasing CAR-T cells and anti-PDL1-conjugated platelets. *Nat. Biomed. Eng.* **5**, 1038–1047 (2021).
3. X. Ji, D. Guo, J. Ma, M. Yin, Y. Yu, C. Liu, Y. Zhou, J. Sun, Q. Li, N. Chen, C. Fan, H. Song, Epigenetic remodeling hydrogel patches for multidrug-resistant triple-negative breast cancer. *Adv. Mater.* **33**, e2100949 (2021).
4. Y. Guo, J. Bae, Z. Fang, P. Li, F. Zhao, G. Yu, Hydrogels and hydrogel-derived materials for energy and water sustainability. *Chem. Rev.* **120**, 7642–7707 (2020).
5. P. Xue, H. K. Bisoyi, Y. Chen, H. Zeng, J. Yang, X. Yang, P. Lv, X. Zhang, A. Priimagi, L. Wang, X. Xu, Q. Li, Near-infrared light-driven shape-morphing of programmable anisotropic hydrogels enabled by MXene nanosheets. *Angew. Chem. Int. Ed. Engl.* **60**, 3390–3396 (2021).
6. H. Na, Y.-W. Kang, C. S. Park, S. Jung, H.-Y. Kim, J.-Y. Sun, Hydrogel-based strong and fast actuators by electroosmotic turgor pressure. *Science* **376**, 301–307 (2022).
7. Y. Ohm, C. Pan, M. J. Ford, X. Huang, J. Liao, C. Majidi, An electrically conductive silver–polyacrylamide–alginate hydrogel composite for soft electronics. *Nat. Electron.* **4**, 185–192 (2021).
8. G. Su, S. Yin, Y. Guo, F. Zhao, Q. Guo, X. Zhang, T. Zhou, G. Yu, Balancing the mechanical, electronic, and self-healing properties in conductive self-healing hydrogel for wearable sensor applications. *Mater. Horiz.* **8**, 1795–1804 (2021).
9. X. Dong, X. Guo, Q. Liu, Y. Zhao, H. Qi, W. Zhai, Strong and tough conductive organo-hydrogels via freeze-casting assisted solution substitution. *Adv. Funct. Mater.* **32**, 2203610 (2022).
10. X. Zhao, X. Chen, H. Yuk, S. Lin, X. Liu, G. Parada, Soft materials by design: Unconventional polymer networks give extreme properties. *Chem. Rev.* **121**, 4309–4372 (2021).
11. Y. Zhou, C. Wan, Y. Yang, H. Yang, S. Wang, Z. Dai, K. Ji, H. Jiang, X. Chen, Y. Long, Highly stretchable, elastic, and ionic conductive hydrogel for artificial soft electronics. *Adv. Funct. Mater.* **29**, 1806220 (2019).
12. Z. Lei, P. Wu, A supramolecular biomimetic skin combining a wide spectrum of mechanical properties and multiple sensory capabilities. *Nat. Commun.* **9**, 1134 (2018).
13. D. Gan, Z. Huang, X. Wang, L. Jiang, C. Wang, M. Zhu, F. Ren, L. Fang, K. Wang, C. Xie, X. Lu, Graphene oxide-templated conductive and redox-active nanosheets incorporated hydrogels for adhesive bioelectronics. *Adv. Funct. Mater.* **30**, 1907678 (2020).
14. S. R. Shin, R. Farzad, A. Tamayol, V. Manoharan, P. Mostafalu, Y. S. Zhang, M. Akbari, S. M. Jung, D. Kim, M. Comotto, N. Annabi, F. E. Al-Hazmi, M. R. Dokmeci, A. Khademhosseini, A bioactive carbon nanotube-based ink for printing 2D and 3D flexible electronics. *Adv. Mater.* **28**, 3280–3289 (2016).
15. K. H. Lee, Y.-Z. Zhang, H. Kim, Y. Lei, S. Hong, S. Wustoni, A. Hama, S. Inal, H. N. Alshareef, Muscle fatigue sensor based on $Ti_3C_2T_x$ MXene hydrogel. *Small Methods* **5**, e2100819 (2021).
16. X. Li, L. He, Y. Li, M. Chao, M. Li, P. Wan, L. Zhang, Healable, degradable, and conductive MXene nanocomposite hydrogel for multifunctional epidermal sensors. *ACS Nano* **15**, 7765–7773 (2021).
17. X. Luo, L. Zhu, Y.-C. Wang, J. Li, J. Nie, Z. L. Wang, A flexible multifunctional triboelectric nanogenerator based on MXene/PVA hydrogel. *Adv. Funct. Mater.* **31**, 2104928 (2021).
18. Z. Zhao, C. Li, Z. Dong, Y. Yang, L. Zhang, S. Zhuo, X. Zhou, Y. Xu, L. Jiang, M. Liu, Adaptive superamphiphilic organohydrogels with reconfigurable surface topography for programming unidirectional liquid transport. *Adv. Funct. Mater.* **29**, 1807858 (2019).
19. J. Wang, Q. Li, K. Li, X. Sun, Y. Wang, T. Zhuang, J. Yan, H. Wang, Ultra-high electrical conductivity in filler-free polymeric hydrogels toward thermoelectrics and electromagnetic interference shielding. *Adv. Mater.* **34**, e2109904 (2022).
20. Z. Shen, Z. Zhang, N. Zhang, J. Li, P. Zhou, F. Hu, Y. Rong, B. Lu, G. Gu, High-stretchability, ultralow-hysteresis conducting polymer hydrogel strain sensors for soft machines. *Adv. Mater.* **34**, e2203650 (2022).
21. Y. Fang, J. Xu, F. Gao, X. Du, Z. Du, X. Cheng, H. Wang, Self-healable and recyclable polyurethane-polyaniline hydrogel toward flexible strain sensor. *Compos. B Eng.* **219**, 108965 (2021).
22. S. Tang, C. Yu, X. Liu, D. Fu, W. Liao, F. Xu, W. Zhong, 2-Methylimidazole assisted synthesis of nanocrystalline shell reinforced PPy hydrogel with high mechanical and electrochemical performance. *Chem. Eng. J.* **430**, 133033 (2022).
23. R. Dong, P. X. Ma, B. Guo, Conductive biomaterials for muscle tissue engineering. *Biomaterials* **229**, 119584 (2020).
24. I. Y. Kuo, B. E. Ehrlich, Signaling in muscle contraction. *Cold Spring Harb. Perspect. Biol.* **7**, a006023 (2015).
25. M. Hua, S. Wu, Y. Ma, Y. Zhao, Z. Chen, I. Frenkel, J. Strzalka, H. Zhou, X. Zhu, X. He, Strong tough hydrogels via the synergy of freeze-casting and salting out. *Nature* **590**, 594–599 (2021).
26. S. Lin, J. Liu, X. Liu, X. Zhao, Muscle-like fatigue-resistant hydrogels by mechanical training. *Proc. Natl. Acad. Sci. U.S.A.* **116**, 10244–10249 (2019).
27. W. Cui, Y. Zheng, R. Zhu, Q. Mu, X. Wang, Z. Wang, S. Liu, M. Li, R. Ran, Strong tough conductive hydrogels via the synergy of ion-induced cross-linking and salting-out. *Adv. Funct. Mater.* **32**, 2204823 (2022).
28. M. Hua, S. Wu, Y. Jin, Y. Zhao, B. Yao, X. He, Tough-hydrogel reinforced low-tortuosity conductive networks for stretchable and high-performance supercapacitors. *Adv. Mater.* **33**, e2100983 (2021).
29. M. Chen, M. Wu, Y. Chen, A. M. Tucker, A. Jagota, S. Yang, Fast, strong, and reversible adhesives with dynamic covalent bonds for potential use in wound dressing. *Proc. Natl. Acad. Sci. U.S.A.* **119**, e2203074119 (2022).
30. X. Xu, V. V. Jerca, R. Hoogenboom, Bioinspired double network hydrogels: From covalent double network hydrogels via hybrid double network hydrogels to physical double network hydrogels. *Mater. Horiz.* **8**, 1173–1188 (2021).

31. S. Lin, X. Liu, J. Liu, H. Yuk, H.-C. Loh, G. A. Parada, C. Settens, J. Song, A. Masic, G. H. McKinley, X. Zhao, Anti-fatigue-fracture hydrogels. *Sci. Adv.* **5**, eaau8528 (2019).

32. Y. Dong, A. N. Ramey-Ward, K. Salaita, Programmable mechanically active hydrogel-based materials. *Adv. Mater.* **33**, e2006600 (2021).

33. Y. Wang, T. Azaïs, M. Robin, A. Vallée, C. Catania, P. Legriel, G. Pehau-Arnaudet, F. Babonneau, M.-M. Giraud-Guille, N. Nassif, The predominant role of collagen in the nucleation, growth, structure and orientation of bone apatite. *Nat. Mater.* **11**, 724–733 (2012).

34. G. M. Whitesides, B. Grzybowski, Self-assembly at all scales. *Science* **295**, 2418–2421 (2002).

35. S. Ghoshal, P. Denner, S. Stapf, C. Mattea, Structural and dynamical heterogeneities in PVA films induced by evaporation during the formation process. *Chem. Phys. Lett.* **515**, 231–234 (2011).

36. H. Zhu, H. Cao, X. Liu, M. Wang, X. Meng, Q. Zhou, L. Xu, Nacre-like composite films with a conductive interconnected network consisting of graphene oxide, polyvinyl alcohol and single-walled carbon nanotubes. *Mater. Des.* **175**, 107783 (2019).

37. Z. Huang, G. Yang, J. Zhang, S. Gray, Z. Xie, Dual-layer membranes with a thin film hydrophilic MOF/PVA nanocomposite for enhanced antiwetting property in membrane distillation. *Desalination* **518**, 115268 (2021).

38. S. Wan, X. Li, Y. Chen, N. Liu, Y. Du, S. Dou, L. Jiang, Q. Cheng, High-strength scalable MXene films through bridging-induced densification. *Science* **374**, 96–99 (2021).

39. K. Chen, X. Tang, B. Jia, C. Chao, Y. Wei, J. Hou, L. Dong, X. Deng, T. H. Xiao, K. Goda, L. Guo, Graphene oxide bulk material reinforced by heterophase platelets with multiscale interface crosslinking. *Nat. Mater.* **21**, 1121–1129 (2022).

40. V. Kochkodan, N. B. Darwish, N. Hilal, The chemistry of boron in water, in *Boron Separation Processes* (Elsevier Inc., 2015), pp. 35–63.

41. C.-E. Kim, K. G. Ray, D. F. Bahr, V. Lordi, Electronic structure and surface properties of $MgB_2(0001)$ upon oxygen adsorption. *Phys. Rev. B* **97**, 195416 (2018).

42. T. Li, Q. Liu, J. Cao, S. W. Gan, X. Dong, C. C. Yen, C. Wu, W. Zhai, A universal chelation-induced selective demetallization strategy for bioceramic nanosheets (BCene). *Nano Lett.* **23**, 7709–7715 (2023).

43. R. P. Vasquez, C. U. Jung, M.-S. Park, H.-J. Kim, J. Y. Kim, S.-I. Lee, X-ray photoemission study of MgB_2. *Phys. Rev. B* **64**, 052510 (2001).

44. O. Karaahmet, B. Cicek, Effect of mechanically modification process on boron carbide synthesis from polymeric precursor method. *Ceram. Int.* **48**, 11940–11952 (2022).

45. I. Yanase, R. Ogawara, H. Kobayashi, Synthesis of boron carbide powder from polyvinyl borate precursor. *Mater. Lett.* **63**, 91–93 (2009).

46. W. Wu, X. Wen, Z. L. Wang, Taxel-addressable matrix of vertical-nanowire piezotronic transistors for active and adaptive tactile imaging. *Science* **340**, 952–957 (2013).

47. J.-Y. Sun, X. Zhao, W. R. K. Illeperuma, O. Chaudhuri, K. H. Oh, D. J. Mooney, J. J. Vlassak, Z. Suo, Highly stretchable and tough hydrogels. *Nature* **489**, 133–136 (2012).

48. H. Wang, U. Ail, R. Gabrielsson, M. Berggren, X. Crispin, Ionic seebeck effect in conducting polymers. *Adv. Energy Mater.* **5**, 1500044 (2015).

49. J. E. B. Randles, Kinetics of rapid electrode reactions. *Discuss. Faraday Soc.* **1**, 11–19 (1947).

50. X. Liang, G. Chen, S. Lin, J. Zhang, L. Wang, P. Zhang, Y. Lan, J. Liu, Bioinspired 2D isotropically fatigue-resistant hydrogels. *Adv. Mater.* **34**, e2107106 (2022).

51. X. Rui-Hong, R. Peng-Gang, H. Jian, R. Fang, R. Lian-Zhen, S. Zhen-Feng, Preparation and properties of graphene oxide-regenerated cellulose/polyvinyl alcohol hydrogel with pH-sensitive behavior. *Carbohydr. Polym.* **138**, 222–228 (2016).

52. W. Zhang, J. Ma, W. Zhang, P. Zhang, W. He, J. Chen, Z. Sun, A multidimensional nanostructural design towards electrochemically stable and mechanically strong hydrogel electrodes. *Nanoscale* **12**, 6637–6643 (2020).

53. Y. Feng, H. Liu, W. Zhu, L. Guan, X. Yang, A. V. Zvyagin, Y. Zhao, C. Shen, B. Yang, Q. Lin, Muscle-inspired MXene conductive hydrogels with anisotropy and low-temperature tolerance for wearable flexible sensors and arrays. *Adv. Funct. Mater.* **31**, 2105264 (2021).

54. Y. Li, J. Yan, Y. Liu, X. M. Xie, Super tough and intelligent multibond network physical hydrogels facilitated by $Ti_3C_2T_x$ MXene nanosheets. *ACS Nano* **16**, 1567–1577 (2022).

55. F. Yang, J. Zhao, W. J. Koshut, J. Watt, J. C. Riboh, K. Gall, B. J. Wiley, A synthetic hydrogel composite with the mechanical behavior and durability of cartilage. *Adv. Funct. Mater.* **30**, 2003451 (2020).

56. M. T. I. Mredha, Y. Z. Guo, T. Nonoyama, T. Nakajima, T. Kurokawa, J. P. Gong, A facile method to fabricate anisotropic hydrogels with perfectly aligned hierarchical fibrous structures. *Adv. Mater.* **30**, 1704937 (2018).

57. M. T. I. Mredha, H. H. Le, V. T. Tran, P. Trtik, J. Cui, I. Jeon, Anisotropic tough multilayer hydrogels with programmable orientation. *Mater. Horiz.* **6**, 1504–1511 (2019).

58. S. Gupta, S. Goswami, A. Sinha, A combined effect of freeze–thaw cycles and polymer concentration on the structure and mechanical properties of transparent PVA gels. *Biomed. Mater.* **7**, 015006 (2012).

59. W. Chen, D. Li, Y. Bu, G. Chen, X. Wan, N. Li, Design of strong and tough methylcellulose-based hydrogels using kosmotropic Hofmeister salts. *Cellul.* **27**, 1113–1126 (2020).

60. Y. Yang, X. Wang, F. Yang, H. Shen, D. Wu, A universal soaking strategy to convert composite hydrogels into extremely tough and rapidly recoverable double-network hydrogels. *Adv. Mater.* **28**, 7178–7184 (2016).

61. H. Ding, Z. Wu, H. Wang, Z. Zhou, Y. Wei, K. Tao, X. Xie, J. Wu, An ultrastretchable, high-performance, and crosstalk-free proximity and pressure bimodal sensor based on ionic hydrogel fibers for human-machine interfaces. *Mater. Horiz.* **9**, 1935–1946 (2022).

62. G. Ge, Y. Zhang, J. Shao, W. Wang, W. Si, W. Huang, X. Dong, Stretchable, transparent, and self-patterned hydrogel-based pressure sensor for human motions detection. *Adv. Funct. Mater.* **28**, 1802576 (2018).

63. Z. Shen, X. Zhu, C. Majidi, G. Gu, Cutaneous ionogel mechanoreceptors for soft machines, physiological sensing, and amputee prostheses. *Adv. Mater.* **33**, e2102069 (2021).

64. V. Amoli, J. S. Kim, E. Jee, Y. S. Chung, S. Y. Kim, J. Koo, H. Choi, Y. Kim, D. H. Kim, A bioinspired hydrogen bond-triggered ultrasensitive ionic mechanoreceptor skin. *Nat. Commun.* **10**, 4019 (2019).

65. C. M. Boutry, M. Negre, M. Jorda, O. Vardoulis, A. Chortos, O. Khatib, Z. Bao, A hierarchically patterned, bioinspired e-skin able to detect the direction of applied pressure for robotics. *Sci. Robot.* **3**, eaau6914 (2018).

66. Y. Wang, H. Wu, L. Xu, H. Zhang, Y. Yang, Z. L. Wang, Hierarchically patterned self-powered sensors for multifunctional tactile sensing. *Sci. Adv.* **6**, eabb9083 (2020).

67. X. Yu, H. Zhang, Y. Wang, X. Fan, Z. Li, X. Zhang, T. Liu, Highly stretchable, ultra-soft, and fast self-healable conductive hydrogels based on polyaniline nanoparticles for sensitive flexible sensors. *Adv. Funct. Mater.* **32**, 2204366 (2022).

68. X. Di, J. Hou, M. Yang, G. Wu, P. Sun, A bio-inspired, ultra-tough, high-sensitivity, and anti-swelling conductive hydrogel strain sensor for motion detection and information transmission. *Mater. Horiz.* **9**, 3057–3069 (2022).

69. Y. Wang, M. Tebyetekerwa, Y. Liu, M. Wang, J. Zhu, J. Xu, C. Zhang, T. Liu, Extremely stretchable and healable ionic conductive hydrogels fabricated by surface competitive coordination for human-motion detection. *Chem. Eng. J.* **420**, 127637 (2021).

70. H. Sun, Y. Zhao, S. Jiao, C. Wang, Y. Jia, K. Dai, G. Zheng, C. Liu, P. Wan, C. Shen, Environment tolerant conductive nanocomposite organohydrogels as flexible strain sensors and power sources for sustainable electronics. *Adv. Funct. Mater.* **31**, 2101696 (2021).

71. C.-Z. Hang, X.-F. Zhao, S.-Y. Xi, Y.-H. Shang, K.-P. Yuan, F. Yang, Q.-G. Wang, J.-C. Wang, D. W. Zhang, H.-L. Lu, Highly stretchable and self-healing strain sensors for motion detection in wireless human-machine interface. *Nano Energy* **76**, 105064 (2020).

72. C. M. Tringides, N. Vachicouras, I. de Lázaro, H. Wang, A. Trouillet, B. R. Seo, A. Elosegui-Artola, F. Fallegger, Y. Shin, C. Casiraghi, K. Kostarelos, S. P. Lacour, D. J. Mooney, Viscoelastic surface electrode arrays to interface with viscoelastic tissues. *Nat. Nanotechnol.* **16**, 1019–1029 (2021).

73. T. G. Yun, M. Park, D. H. Kim, D. Kim, J. Y. Cheong, J. G. Bae, S. M. Han, I. D. Kim, All-transparent stretchable electrochromic supercapacitor wearable patch device. *ACS Nano* **13**, 3141–3150 (2019).

74. V. R. Feig, H. Tran, M. Lee, Z. Bao, Mechanically tunable conductive interpenetrating network hydrogels that mimic the elastic moduli of biological tissue. *Nat. Commun.* **9**, 2740 (2018).

75. X. Ren, X. Yang, T. Yang, X. Cu, Y. Ye, X. Wu, X. Zheng, B. Wang, Y. Wan, Z. Luo, Highly conductive PPy-PEDOT:PSS hybrid hydrogel with superior biocompatibility for bioelectronics application. *ACS Appl. Mater. Interfaces* **13**, 25374–25382 (2021).

76. Y. Cheng, J. Zang, X. Zhao, H. Wang, Y. Hu, Nanocellulose-enhanced organohydrogel with high-strength, conductivity, and anti-freezing properties for wearable strain sensors. *Carbohydr. Polym.* **277**, 118872 (2022).

77. L. Wang, W. A. Daoud, Hybrid conductive hydrogels for washable human motion energy harvester and self-powered temperature-stress dual sensor. *Nano Energy* **66**, 104080 (2019).

78. M. Yang, X. Ren, T. Yang, C. Xu, Y. Ye, Z. Sun, L. Kong, B. Wang, Z. Luo, Polypyrrole/sulfonated multi-walled carbon nanotubes conductive hydrogel for electrochemical sensing of living cells. *Chem. Eng. J.* **418**, 129483 (2021).